Control of VSC-HVDC with Electromechanical Characteristics and Unified Primary Strategy

Weiyi Zhang[1], Kumars Rouzbehi[1], J. Ignacio Candela[1]
[1]Department of Electrical Engineering
Technical University of Catalonia
Barcelona, Spain, 08222
Email: weiyi.zhang@estudiant.upc.edu

Alvaro Luna[1], Pedro Rodriguez[1,2]
[2]Abengoa Research
Abengoa
Sevilla, Spain, 41014

***Abstract*—High voltage dc (HVDC) systems act as the prevailed solution for transmitting offshore wind energy to onshore main grids. Control of the voltage source converters (VSC) in HVDC systems is decisive for the performance.**

This paper proposes the control of VSC-HVDC with electromechanical characteristics and unified primary strategy, as a reaction to the updated requirements of the ac grid transmission system operators. As two important aspects of VSC-HVDC control, converter control and primary control are both designed in detail. Electromechanical characteristics make the VSC capable of providing inertia to the ac networks as well as simplicity in island operation. Besides, unified primary control is given as a universal primary strategy for VSC stations, and especially takes into account frequency support and control mode transition. The proposed converter control is validated in scaled-down 10 kW laboratory setups, while the proposed primary control is endorsed by the simulation tests on a CIGRE multi-terminal HVDC model.

I. INTRODUCTION

For the past decade, high voltage dc (HVDC) transmission systems based on voltage source converters (VSC) have emerged as a promising technology due to its technical and economic advantages in different applications compared with the traditional systems based on line commuted converters (LCC) [1].

In HVDC systems, offshore VSCs normally perform power/frequency control, while onshore VSCs control the dc voltage. In this manner the balance of energy is achieved and the power is transmitted from the offshore to the ac network following the wind status. However, with expected increasing integration of HVDC systems, their impact on the power system stability, especially the frequency stability, will be more visible. Therefore, frequency support and inertia emulation should be considered in the control design of future VSC-HVDC.

VSC-HVDC control with inertia emulation has been being discussed in recent years. The authors in [2] define the power-frequency swing based on inertia, and link the offshore frequency, dc voltage and onshore frequency by droop control. In this way the offshore grids can provide the specified amount of inertia to stabilize the frequency perturbations in the onshore grids. In [3], inertia emulation control of VSC-HVDC is also designed, in which the dc voltage is regulated following the ac frequency in a specified trajectory based on the inertia characteristics, and the energy stored on the dc bus acts as the inertia reserve. Besides, VSC control design with inertia emulation and virtual admittance is seen in [4] for supporting low-inertia island grid.

Regarding primary control of VSC-HVDC, voltage droop control is frequently used. The operation of HVDC systems with voltage droop characteristics is critical for the system stability. The droop slope can be specified considering the steady-state voltage range of the dc grid and the power processing constraint that is applied to each VSC [5]. Since the HVDC systems are interfaced with ac systems, the requirements of the ac transmission system operators (TSO) should also be met. Frequency support is hence necessary for control design of future onshore VSCs. A secondary control structure for multi-terminal HVDC (MTDC) grids with load frequency control is proposed in [6], thus the power order of VSC can hence be set taking into account the ac grid frequency. The frequency support can also be achieved by configuring the primary control as shown in [7].

Conventionally, the VSC stations in HVDC systems are devoted to the stabilization of the dc systems, and simply act as feeders to the ac systems. In contrast, this paper addresses the control of VSC-HVDC considering the ac TSO requirements as well as the stabilization of dc systems. The proposal can be divided into two aspects, the converter control and primary control. Regarding the converter control, the VSCs are equipped with electromechanical characteristics (the emulation of inertia, damping and output impedance of synchronous machines). For primary control, a universal structure is designed with multiple modes of operation (including frequency droop) and availability of mode transition for flexible and autonomous operation. The proposed control is validated by simulation and scaled-down experimental results.

II. PROPOSED CONTROL FOR VSC-HVDC

A VSC based on the proposed control strategy is shown in Fig. 1. Electromechanical block and unified primary controller are the two main features of the proposed control.

A. Converter control

The inertia emulation block is designed in detail in section III. It is able to generate a virtual synchronous frequency ω,

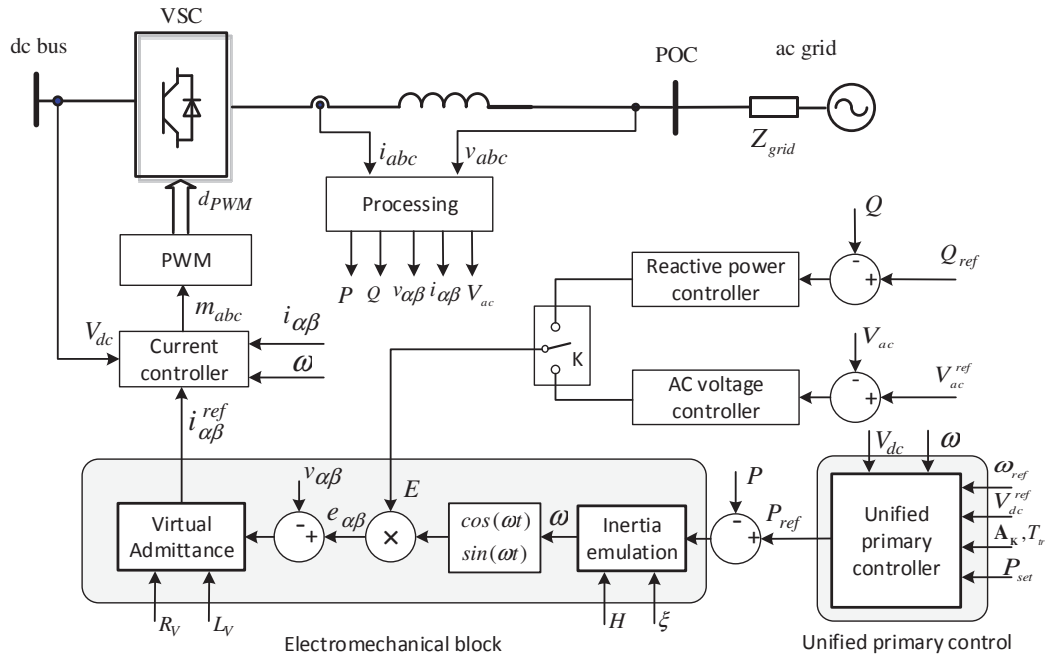

Fig. 1. Control of VSC-HVDC with virtual electromechanical characteristics and unified primary strategy.

which is integrated to a phase signal θ. Combining the phase signal θ and the magnitude signal U_{ref} generated by the reactive power controller, the virtual electromotive force e can be generated.

Unlike proposals that implement inertia through a phase-locked loop (PLL) [8], [9], the proposed control incorporates inertia in the power loop controller and makes the VSC synchronized to the grid through power angle synchronization instead of voltage phase synchronization. The control dynamics are not affected by the dynamics of the PLL. In addition, the inertial effect is not dependent on the connection to an external grid.

In this paper, the virtual admittance structure adopted in [10] is selected as the structure of the inner control loops to emulate the output impedance of synchronous machines. By presenting a reactance and a damping resistance that are both adjustable, it will play a key role when performing load sharing and presents a natural voltage magnitude droop feature for grid voltage support. The use of a back-up PLL as in [11] for start-up or severe fault conditions is not necessary thanks to the adjustable virtual admittance, which avoids the complexity in the control design.

B. Primary control

VSC stations in MTDC systems can operate in different modes, where different primary strategies are used. The most adopted operational modes for VSC include dc voltage (V_{dc}) control, frequency (f) control, and voltage oriented droop control. When the VSC connects to onshore ac grids, it commonly works in V_{dc} control mode or voltage-oriented droop mode, and has not response to the ac grid frequency. Ever since the beginning of the study on MTDC grids, this decoupling feature has always been favored because of the capability of isolating the perturbation or fault in one ac grid, thus avoid the complication or instability of the ac/dc grids.

However, with the increasing installation of MTDC systems, ancillary services for both ac and dc grids are expected [12], and the support to ac grid frequency is becoming more interesting, especially in cases when significant amount of MTDC systems are integrated to the main ac system or when the connected ac grid has low inertia. Therefore, control modes with P-f or V_{dc}-f interaction are required.

The unified primary controller shown in Fig. 1 integrates all the aforementioned operation modes to a unified control structure, which can be used for all the VSC stations. The operation mode of VSC can be dispatched or switched via scheduling the control parameters. The detailed design is given in section IV.

III. Electromechanical Characteristics

The modeling of the active power control loop is shown in Fig. 2.

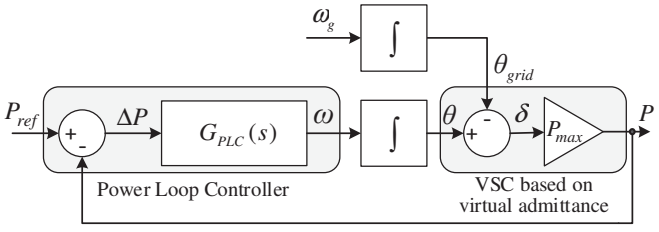

Fig. 2. Modeling of active power control.

According to the electrical characteristics of the synchronous machines, the generated active power can be approximated to (1), considering a small signal model and the fact that the output impedance of a synchronous generator is mainly inductive.

$$\Delta P = P_{\max} \Delta \delta \tag{1}$$

where ΔP is the incremental generated power in three phases, and $\Delta\delta$ the incremental phase-angle difference between the virtual electromotive force e and the grid voltage v. The admittance gain is expressed as,

$$P_{\max} = \frac{EV}{X} \tag{2}$$

where E and V are respectively the phase-to-phase RMS of virtual electromotive force, e, and the grid voltage, v, and X is the output reactance, which is provided by the virtual admittance.

The synchronous angular speed ω is adjusted according to the error in power regulation, and will further move the load angle to regulate the power. In this way, even if the grid voltage angle θ_{grid} is unknown and can be variable in realistic operation, ω can always be adjusted to diminish the power control error, and meanwhile maintains the synchronization with the grid frequency ω_g.

A. *Implementation of Swing Equation*

The power loop controller can be designed as a replication of the swing equation of synchronous machine, and the transfer function is shown as,

$$G_{PLC}(s) = \frac{\omega_s}{2HS_N s + \omega_s^2 D} \tag{3}$$

where ω_s is the synchronous angular frequency, H the inertia constant, D the damping parameter and S_N the nominal power of the VSC. For synchronous machines, even if the damper winding can provide damping, it is limited by some mechanical and electrical constraints. When the swing equation is virtually implemented as (3), the damping of the power loop can be improved and optimized by means of tuning D.

Based on (3), the resulting closed-loop transfer function is obtained and shown in (4a).

$$\frac{\partial P}{\partial P_{ref}}(s) = \frac{\omega_n^2}{s^2 + 2\xi\omega_n s + \omega_n^2} \tag{4a}$$

$$\xi = \frac{D\omega_s}{2}\sqrt{\frac{\omega_s}{2HS_N P_{\max}}} \tag{4b}$$

$$\omega_n = \sqrt{\frac{P_{\max}\omega_s}{2HS_N}} \tag{4c}$$

Equation (4a) is given in the specific form as an analogy of the second order parametric transfer function, for which the time response is defined by the parameters ω_n and ξ. Moreover, ω_n and ξ are also linked to the damping and inertia parameters of the swing equation through (4b) and (4c). And to guarantee the stability of the system, ξ has to be specified greater than 0.

Other than the response to power reference changes, the response to frequency disturbances also needs to be studied for analyzing the dynamics of the power loop. In the modeling, the grid frequency can be linked to the grid phase angle by an integrator, as shown in Fig. 2. Then taking grid frequency as the variable and taking the output power as the function, the transfer function is shown as,

$$\frac{\partial P}{\partial \omega_g}(s) = \frac{-P_{\max}(s + 2\xi\omega_n)}{s^2 + 2\xi\omega_n s + \omega_n^2} \tag{5}$$

The response shown in (5) incorporates a steady-state droop slope which is expressed as,

$$D_P = \left|\frac{\partial P}{\partial \omega_g}(0)\right| = \frac{2\xi P_{\max}}{\omega_n} \tag{6}$$

Normally, the grid frequency deviation percentage that extracts the full rated power from the converter is used as the indicator of the droop slope, which is represented by $1/R_D$. The relation between R_D and D_P is shown as,

$$R_D = \frac{D_P \omega_s}{S_N} \tag{7}$$

Substituting the D_P in (7) using (6) and denoting ω_n using (4c), the interaction among inertia, damping and droop slope is obtained as,

$$\frac{1}{R_D} = \frac{1}{2\xi}\sqrt{\frac{S_N}{2HP_{\max}\omega_s}} \tag{8}$$

Since the per unit value of the power transmission reactance X_{pu} can be expressed as,

$$X_{pu} = \frac{X}{EV/S_N} = \frac{S_N}{P_{\max}} \tag{9}$$

Equation (8) can be transformed into (10).

$$\frac{1}{R_D} = \frac{1}{2\xi}\sqrt{\frac{X_{pu}}{2H\omega_s}} \tag{10}$$

Equation (10) shows the constraint among H, ξ, X_{pu} and $1/R_D$. And since the values of H and X_{pu} are normally pre-fixed considering the design requirement in inertia emulation and load sharing, the challenge mainly lies in the constraint between ξ and $1/R_D$.

This constraint is visualized in Fig. 3, where H is specified to be 0.3, 0.6, 5 and 20 respectively in four cases, and the grid nominal frequency is set to 50 Hz and X_{pu} is set to 0.3 to specify the model.

As shown in Fig. 3, once the droop slope is fixed, the damping coefficient will be fixed as well. For traditional synchronous machines, 4% is a typical value for the droop slope. But for RES-based generation plants, $1/R_D$ may have to be greater taking into account the power reserve that is technically

and economically feasible. In the scenarios shown in Fig. 5, if $1/R_D$ is fixed to 4%, ξ will be below 0.5, which can be insufficient for the damping performance. If $1/R_D$ is required to be greater, ξ has to be further reduced.

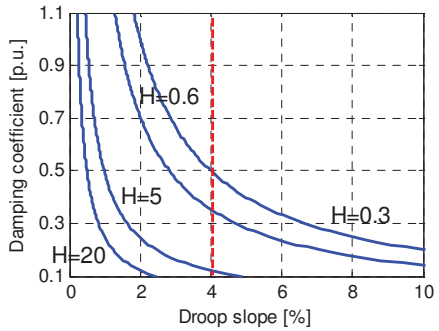

Fig. 3. The relation between the droop slope $1/R_D$ and the damping coefficient ξ.

As shown in (10), in order to present inertia and damping features, $1/R_D$ is not able to reach the infinite. It means that the droop characteristics intrinsically exist in the power loop.

B. PI-based Power Loop Controller

As explained in section III.A, if the power loop controller is designed as (3) for a replication of the swing equation, an inherent *P-f* droop will be introduced. In order to eliminate the inherent *P-f* droop and only let the primary control block determine the droop characteristics, the commonly used PI controller shown in (11) is used as the power loop controller in this paper.

$$G_{PLC}(s) = K_X + \frac{K_H}{s} \tag{11}$$

Compared with the previous design, the PI-based power loop controller is able to fix the regulated power to the reference value in steady state even if there are variations in the grid frequency. In this way, the parameter setting of the primary droop controller is straightforward and simple, since the power loop does not incorporate intrinsic droop. Moreover, by properly setting the gains of the PI controller, the inertia and damping characteristics can still be given.

Substituting expression (11) for the power loop controller block in Fig. 4, the resulting closed-loop transfer function is shown in (12a), which is still a second order transfer function and the dynamics can easily be analyzed. The damping coefficient and natural frequency are respectively expressed in (12b) and (12c).

$$\frac{\partial P}{\partial P_{ref}}(s) = \frac{2\xi\omega_n s + \omega_n^2}{s^2 + 2\xi\omega_n s + \omega_n^2} \tag{12a}$$

$$\xi = \frac{P_{max} K_X}{2\omega_n} \tag{12b}$$

$$\omega_n = \sqrt{P_{max} K_H} \tag{12c}$$

Even though (12a) has a different expression in the numerator compared with the standard second order parametric transfer function, the denominator of the system is unchanged. Therefore, in order to place the closed-loop poles in the left half plain to guarantee the stability, ξ still has to be specified greater than 0.

According to (12b) and (12c), by specifying the control parameters K_X and K_H, the damping and inertia characteristics can be respectively given.

The response of power in presence of grid frequency disturbances (*P-f* response) is shown in (13),

$$\frac{\partial P}{\partial \omega_g}(s) = \frac{-P_{\max} s}{s^2 + 2\xi\omega_n s + \omega_n^2} \tag{13}$$

from which the steady-state droop slope is obtained as (14).

$$D_P = \left| \frac{\partial P}{\partial \omega_g}(0) \right| = 0 \tag{14}$$

This equation indicates that the generated power will always track the power reference in steady state regardless of the frequency variations.

IV. Unified Primary Control

The structure of the unified primary controller is shown in detail in Fig. 4. P_{set} is the power order from the power flow program, and $\mathbf{A_K}$ is the parameter matrix shown in (15).

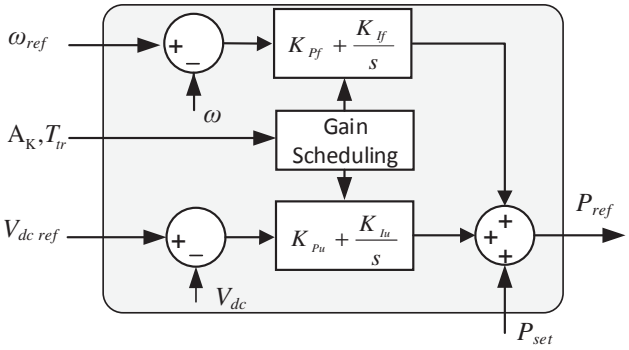

Fig. 4. Unified primary controller.

$$\mathbf{A_K} = \begin{bmatrix} K_{Pf} & K_{If} \\ K_{Pu} & K_{Iu} \end{bmatrix} \tag{15}$$

It is worth noting that the matrix $\mathbf{A_K}$ will always contain zero element to avoid control fighting, and it will be specified by the secondary commands. With different configuration in $\mathbf{A_K}$, the unified reference controller performs different functions, thus assign the required operation mode to the controlled VSC. And for some operation modes, P_{set} needs to be set to zero. The secondary control also specifies the transition time T_{tr}, and the gain scheduling block will adjust $\mathbf{A_K}$ to the objective during the transition time.

Except for the fixed power control, other operation modes can be selected and are generalized as follow,

- Mode A: *f* control: $K_{Pf} \neq 0$, $K_{If} \neq 0$, $K_{Pu}=0_P$, $K_{Iu}=0$.

$$P_{ref} = \left(K_{Pf} + \frac{K_{If}}{s}\right)\left(f_{ref} - f\right) \tag{16}$$

- Mode B: P-V_{dc} droop control: K_{Pf}= 0, K_{If}=0, K_{Pu}≠0, K_{Iu}=0.

$$P_{ref} = P_{set} + K_{Pu}(V_{dc} - V_{dc\,ref}) \quad (17)$$

- Mode C: V_{dc} control: K_{Pf}=0, K_{If}=0, K_{Pu}≠0P, K_{Iu}≠0.

$$P_{ref} = \left(K_{Pu} + \frac{K_{Iu}}{s}\right)\left(V_{dc} - V_{dc\,ref}\right) \quad (18)$$

- Mode D: P-f droop control: K_{Pf}≠ 0, K_{If}=0, K_{Pu}=0, K_{Iu}=0.

$$P_{ref} = P_{set} + K_{Pf}\left(f_{ref} - f\right) \quad (19)$$

- Mode E: V_{dc}-f control: K_{Pf}≠0, K_{If}=0, K_{Pu}≠0P, K_{Iu}=0.

$$P_{ref} = P_{set} + K_{Pf}\left(f_{ref} - f\right) + K_{Pu}\left(V_{dc} - V_{dc\,ref}\right) \quad (20)$$

V. Results

Scaled-down experimental results are obtained from a 10 kW laboratory VSC connected to a 400 V ac grid to show the electromechanical characteristics. Further, simulation results based on CIGRE benchmark validate the proposed primary control.

A. Electromechanical characteristics

The structure of the experimental system is shown in Fig. 5(a), and a view of the setups is given in Fig. 5(b).

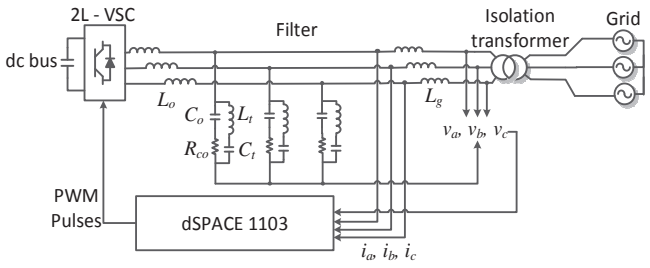

(a)

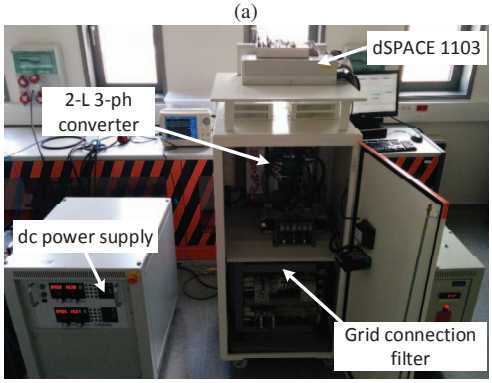

(b)

Fig. 5. Scaled-down 10 kW experimental system: (a) configuration, (b) setups.

The dc bus is supplied by a 40 kW dc power source, by which the dc bus voltage is fixed for providing sufficient power reserve. The ac grid is formed by a regenerative power source, by which the voltage magnitude and frequency can be specified and adjusted. The control algorithm is implemented in a dSPACE 1103. The key parameters of the setups and the controller are shown in Table I. For an easy evaluation and comparison of the experimental results, all the tests are done under the same value in damping coefficient ξ, which is fixed to 0.73. The primary control block is disabled in the test.

TABLE I
Key Experimental Tests Parameters

Symbol	Definition	Value
V_{DC}	dc-link voltage [V]	640
V_g	grid phase-to-phase voltage RMS [V]	400
f_g	grid nominal frequency [Hz]	50
S_N	nominal power [kW]	10
f_{sw}	switching frequency [Hz]	10050
ξ	damping coefficient [p.u.]	0.73
R_{pu}	virtual resistance [p.u.]	0.1
X_{pu}	virtual reactance [p.u.]	0.3

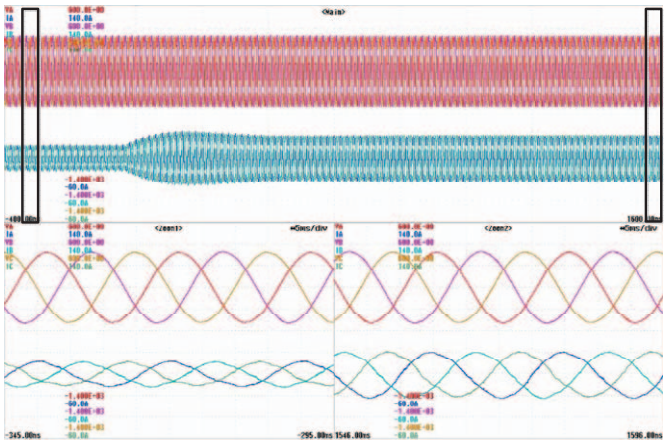

(a)

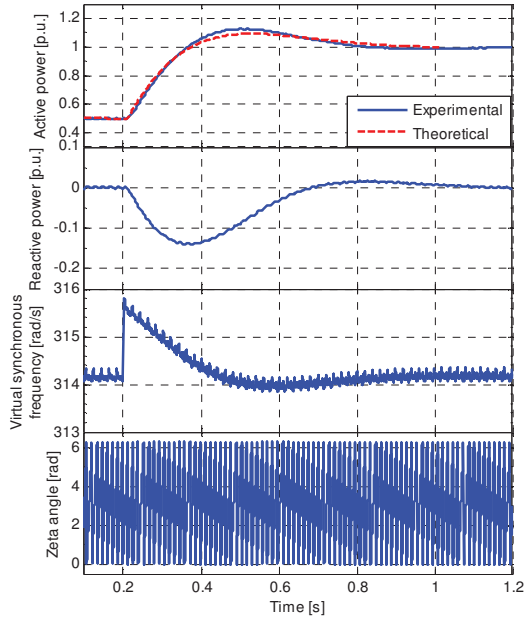

(b)

Fig. 6. Response in presence of power reference step: (a) voltage and current, (b) active and reactive power, controller generated frequency, and phase of electromotive force.

Firstly, a step change in power reference from 0.5 p.u. to 1

p.u. is given to validate the dynamic performance. To clearly show the inertia characteristics, H is designated to be 10 s as a great value. The grid voltage and injected current waveforms are shown in Fig. 6(a), and the active power, reactive power, virtual synchronous frequency ω and the phase of the electro-motive force θ are plotted in Fig. 6(b).

As shown in the results, the grid injected current and power change in a ramp, showing the typical response of a second-order system. The transient response without any oscillations also indicates a proper damping of the system. And in the steady state, the injected active and reactive power is accurately controlled.

The active power profile is compared with the predicted trajectory as shown in Fig. 6(b), and the power response complies with the defined inertia characteristics. The predicted trajectory is calculated by imposing a step input in the transfer function shown in (12a). The virtual synchronous frequency ω is also shown in the figure, and the grid synchronization is well achieved.

Secondly, variations of the grid frequency are imposed by configuring the ac regenerative power source, and the frequency changing slope is made to ±1Hz/s. The response of the injected current, active and reactive power and virtual synchronous frequency are respectively shown in Fig. 7. The active power reference is set to 0.5 p.u. and the reactive power reference to 0, and the inertia constant is kept the same as in the previous test.

According to the results, the injected current and power counteract the deviation of the grid frequency, showing a grid-supporting behavior. The controlled active and reactive power goes back to its reference in steady state, presenting the accurate control of active and reactive power. Besides, the virtual synchronous frequency ω shows an accurate lock of the grid frequency in steady state as well as the inertia dynamics.

B. Validation of unified primary droop

A simulated MTDC grid based on CIGRE WG4-B58 benchmark is built as shown in Fig. 8. The proposed unified primary controller is implemented for each VSC but configured to different operation modes.

In the simulation tests, the grid B0 is configured to be a Thevenin model that leads to a stiff frequency. The VSC Cb-B1 and Cb-B2 are hence assigned with voltage droop control. The offshore VSC stations Cb-C2 and Cb-D1 perform frequency control. The VSC Cb-A1 works in different control modes with different control parameters in the following tests. The control parameters for VSC station Cb-A1 used are shown in Table II. The base power for VSCs and the base voltage for dc buses are 1200 MW and 800 kV, respectively. Two synchronous machines supply the grid A0 with the base power of 400 and 200 MW. They both have the inertia constant 0.5 s.

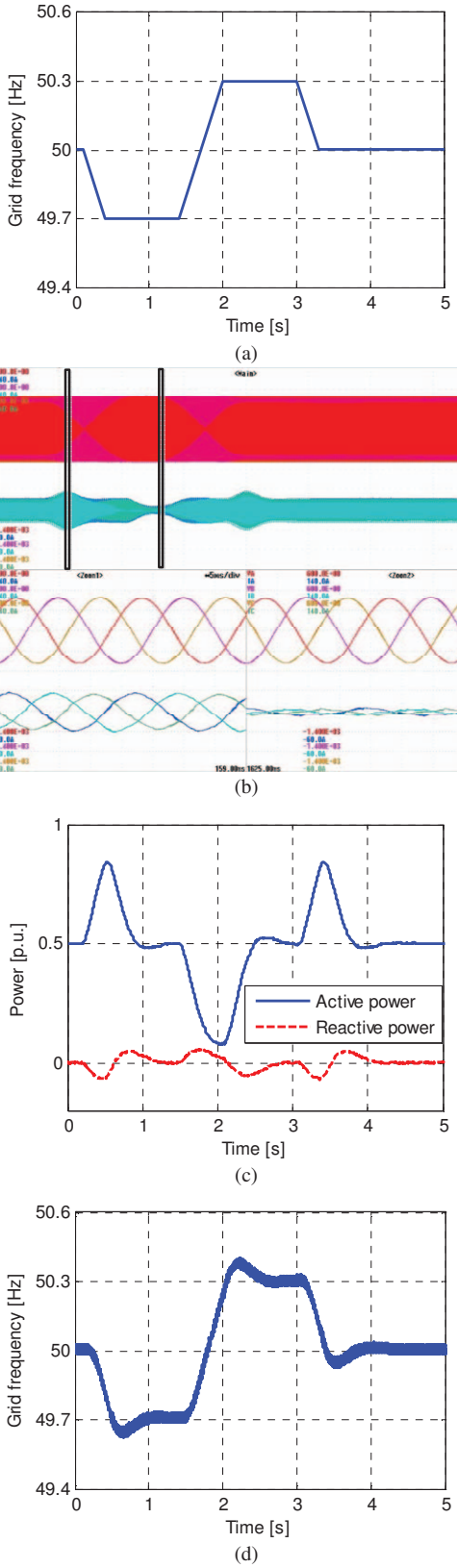

Fig. 7. Response in presence of grid frequency disturbances: (a) grid frequency changes, (b) voltage and current, (c) active and reactive power, (d) controller generated frequency.

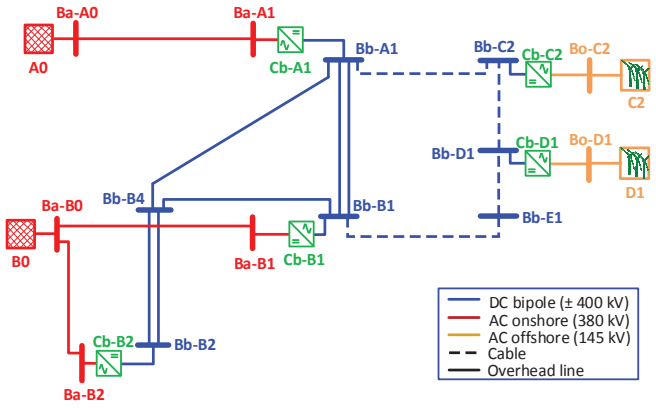

Fig. 8. Simulated plant based on CIGRE WG4-B58 benchmark.

TABLE II
CONTROL PARAMETERS FOR VSC CB-A1

Parameter	K_{PU}	K_{Pf}
A_{K1}	20	0
A_{K2}	20	0.4
A_{K3}	20	0.8
A_{K4}	0	0.4

As the first event, a sudden loss of the mechanical power of the 200-MW synchronous machine takes place, and the results based on different control parameters are shown in Fig. 9. The other generator (400 MW) increases the output power to keep the power equilibrium. And due to the drop of the frequency, the VSC also increases its injected power to contribute to the frequency stabilization, which is companied by the drop of the dc voltage. Comparing different profiles in each scope, it is found that the ac grid supporting effect can be enhanced by increasing the value of K_{Pf}, with the compromise of the dc voltage drop.

In the second event, a step increase of 100 MW in the load on the dc bus Bb-B1s takes place. This event might represents the dc grid perturbations caused by the change of the power import from the offshore wind farms or power injections in one of the onshore terminals. Fig. 10 shows the responses of the ac grid A0 and VSC Cb-A1. Comparing different profiles in each scope, the effect of K_{Pu} and K_{Pf} are both shown, corresponding to the dc and ac droop support. And by specifying different ratios for K_{Pu} over K_{Pf}, the dc voltage droop support and ac frequency droop support can be achieved at different levels.

In order to show the capability of the unified primary controller in smoothly switching among different operation modes (that is needed after a fault and block of one VSC station), the following test is done. The operation mode of VSC Cb-A1 transits from the Mode B (voltage droop control) to Mode E (V_{dc}-f control). The transition starts at 5 s and arrive to the new operation mode during 10 s. The dc voltage and injected active power at each node are seen to move to the new operation point in Fig. 11(a) and (b), respectively. A load change in ac grid A0 takes place at 20 s, and the active power injected by the VSC Cb-A1 shows the response in Fig. 11(c). In contrast, the responses when the VSC works in Mode B are also plotted, and injected active power has not significant responses in presence of ac load changes. Fig. 11(d) shows the effect of the frequency support under the Mode E compared with the Mode B.

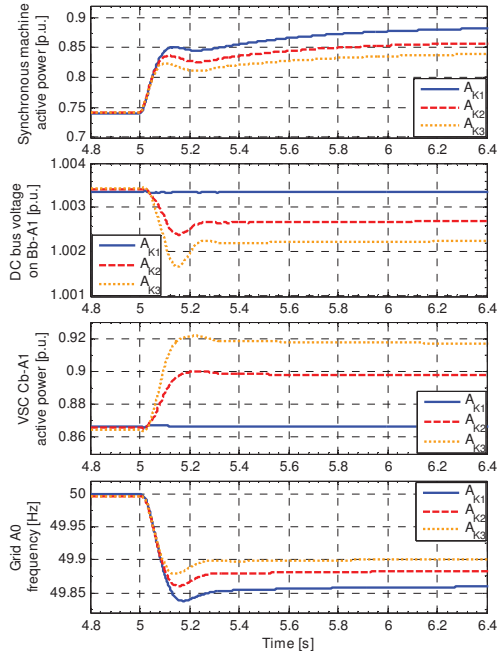

Fig. 9. The response of the MTDC grid after a 200 MW generator lost in grid A0, responses of the other generator in A0 and VSC Cb-A1.

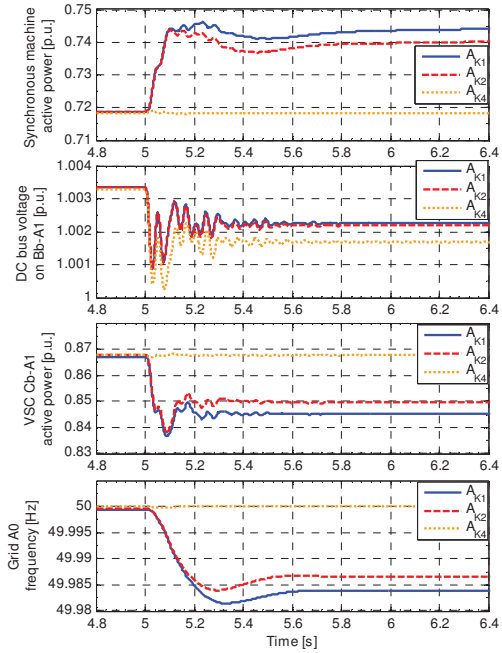

Fig. 10. The response of the MTDC grid when the dc load on Bb-B1s increases in a step.

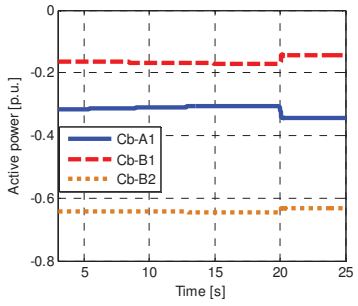

(a)

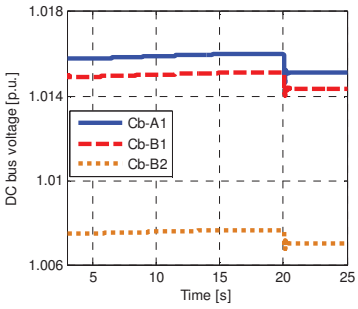

(b)

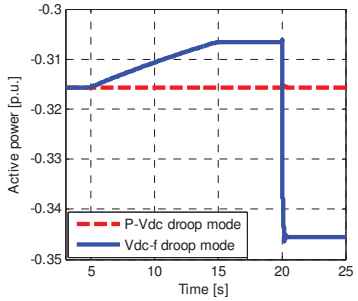

(c)

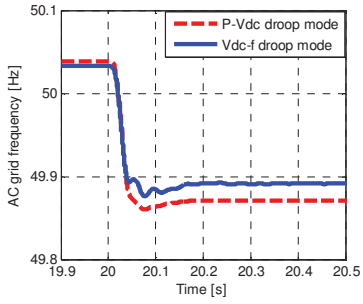

(d)

Fig. 11. Transition from the Mode B to Mode E: (a) active power, (b) dc bus voltage, (c) active power of VSC Cb-A1, (d) A0 grid frequency.

VI. Conclusion

Considering the needs of not only dc but also ac systems, this paper proposes the control of VSC in HVDC systems with electromechanical characteristics and unified primary strategy. The main features of the proposed control include inertia emulation, virtual admittance, frequency droop option in primary control and operation mode transition.

Power reference changes and grid frequency sweep applied in a 10 kW laboratory system are selected as the scenarios to show that the VSC can provide the specified inertia to the ac systems. Besides, the effectiveness of the proposed unified primary controller is also validated in a MTDC simulation model, and the voltage droop, frequency droop and operation mode transition are well achieved.

Acknowledgment

This work has been partially supported by the Spanish Ministry of Economy and Competitiveness under the project ENE2014-60228-R. Any opinions, findings and conclusions or recommendations expressed in this material are those of the authors and do not necessarily reflect those of the host institutions or funders.

References

[1] F. Schettler, H. Huang, and N. Christl, “HVDC transmission systems using voltage sourced converters design and applications,” in *Power Engineering Society Summer Meeting*, 2000, vol. 2, pp. 715–720.

[2] B. Silva, C. L. Moreira, L. Seca, Y. Phulpin, and J. a P. Lopes, “Provision of inertial and primary frequency control services using offshore multiterminal HVDC networks,” *IEEE Trans. Sustain. Energy*, vol. 3, no. 4, pp. 800–808, 2012.

[3] J. Zhu, C. D. Booth, G. P. Adam, A. J. Roscoe, and C. G. Bright, “Inertia emulation control strategy for VSC-HVDC transmission systems,” *IEEE Trans. Power Syst.*, vol. 28, no. 2, pp. 1277–1287, 2013.

[4] W. Zhang, K. Rouzbehi, A. Luna, G. B. Gharehpetian, and P. Rodriguez, “Multi-terminal HVDC grids with inertia mimicry capability,” *IET Renew. Power Gener.*, vol. 10, no. 6, pp. 752–760, 2016.

[5] C. D. Barker and R. Whitehouse, “Autonomous Converter Control in a Multi-terminal HVDC System,” in *9th IET International Conference on ACDC*, 2010, pp. 1–5.

[6] A. Marten and D. Westermann, “Load Frequency Control in an interconnected power system with an embedded HVDC Grid,” in *IEEE Power and Energy Society General Meeting*, 2012, pp. 1–7.

[7] T. M. Haileselassie, R. E. Torres-Olguin, T. K. Vrana, K. Uhlen, and T. Undeland, “Main grid frequency support strategy for VSC-HVDC connected wind farms with variable speed wind turbines,” in *IEEE PES PowerTech*, 2011, pp. 1–6.

[8] M. A. Torres, L. A. Lopes, L. A. Moran, and J. R. Espinoza, “Self-Tuning Virtual Synchronous Machine : A Control Strategy for Energy Storage Systems to Support Dynamic Frequency Control,” *IEEE Trans. Energy Convers.*, vol. 29, no. 4, pp. 833–840, 2014.

[9] H. Alatrash, A. Mensah, E. Mark, G. Haddad, and J. Enslin, “Generator emulation controls for photovoltaic inverters,” *IEEE Trans. Smart Grid*, vol. 3, no. 2, pp. 996–1011, 2012.

[10] P. Rodriguez, I. Candela, C. Citro, J. Rocabert, and A. Luna, “Control of Grid-Connected Power Converters Based on a Virtual Admittance Control Loop,” in *Proc. EPE*, 2013, pp. 1–10.

[11] L. Zhang, L. Harnefors, and H. P. Nee, “Power-synchronization control of grid-connected voltage-source converters,” *IEEE Trans. Power Syst.*, vol. 25, no. 2, pp. 809–820, 2010.

[12] D. Van Hertem and R. H. Renner, “Ancillary services in electric power systems with HVDC grids,” *IET Gener. Transm. Distrib.*, vol. 9, no. 11, pp. 1179–1185, 2015.